

Hexagonal Zero Mode TEM Coil: A Single-Channel Coil Design for Imaging Multiple Small Animals

Jelena Lazovic,¹ Dragan S. Stojkovic,² Christopher M. Collins,¹ Qing X. Yang,¹ J. Thomas Vaughan,³ and Michael B. Smith^{1*}

A novel hexagonal coil design for simultaneous imaging of multiple small animals is presented. The design is based on a coaxial cavity and utilizes the magnetic field formed between two coaxial conductors with hexagonal cross-sections. An analytical solution describing the B_1 field between conductors of the hexagonal coil was found from the Biot-Savart law. Both experimental results and analytical calculations showed a variation in the B_1 field within the imaging region of less than 10%. Numerical calculations predicted ~35% improvement in B_1 field homogeneity with the hexagonal coil design compared to a cylindrical coaxial cavity design. The experimentally-measured signal-to-noise ratio (SNR) of the hexagonal coil loaded with six 50-mM phantoms was only 4–5% lower than that of a single parallel plate resonator loaded with one phantom. In vivo spin-echo (SE) images of six 7-day-old rat pups acquired simultaneously demonstrated sufficient SNR for microimaging. The construction scheme of the coil, simple methods for tuning and matching, and an anesthesia device and animal holder designed for the coil are described. The hexagonal coil design utilizes a single receiver and allows for simultaneous imaging of six small animals with no significant compromise in SNR. Magn Reson Med 53:1150–1157, 2005. © 2005 Wiley-Liss, Inc.

Key words: MRI; multi-animal; RF coil; RF homogeneity; signal-to-noise ratio

There is a growing interest in imaging multiple animals simultaneously to increase throughput and significantly reduce imaging time. In particular, multiple-animal imaging can reduce the total imaging time during kinetics studies that require repetitive experiments and include multiple animals. Fitting multiple animals into a single volume coil can require averaging in order to provide sufficient signal-to-noise ratio (SNR) for the voxel size required for microimaging (1). Previous designs for multiple-animal imaging were based on the use of separate electrically isolated radiofrequency (RF) coils and separate receivers (2,3). The proximity of multiple RF coils and separate receivers inevitably leads to complicated couplings and image artifacts (2,3). Our goal was to develop a single-channel coil capable of imaging multiple animals with

good SNR and homogeneity. We chose a design based on a coaxial geometry (4,5) because the coaxial cavity coil has inherently high sensitivity. Coaxial cavities have been used in previous imaging studies (5), and in methods using the zero mode and the space between inner and outer conductors (4). A traditional cylindrical coaxial cavity coil in the zero mode is associated with a strong B_1 field gradient in the radial direction between the conductors as a consequence of the coaxial geometry (6,7). Strong B_1 field gradients are not desirable, since they lead to nonuniform signal intensity (SI) and contrast in MR images. Ideally, a homogeneous magnetic field is produced between two parallel, infinite planes with current flow in opposite directions. Pairs of parallel plates can be connected, and by connecting the first and last pairs together one can form a coaxial structure. This conformation into a coaxial structure allows the pairs of parallel plates to behave as a single entity resonant cavity with a unique mode of resonance. The magnetic flux is preserved within the cavity and is mutually shared among different pairs of parallel plates. B_1 field homogeneity is improved by replacing the cylindrical with the hexagonal geometry, and replacing the continuous outer conductor with six discontinuous plates.

The hexagonal coil design is intended for in vivo animal studies, and for that purpose we developed an anesthesia manifold to be used with the coil for equal distribution of anesthetics (Fig. 1). For example, imaging with the hexagonal coil allows three control and three treated rat pups to undergo identical experimental conditions. We also developed an animal holder to enable easy positioning of the rats and minimize animal motion during acquisition, as shown in Fig. 1. While the coil size employed here precluded imaging of rat pups older than 9 days, the proposed design can be used to construct larger coils that will accommodate larger animals.

MATERIALS AND METHODS

Hexagonal Coil

The main structural features of the hexagonal coil are shown in Fig. 2. The coil consists of six pairs of parallel copper plates (4.6×2 cm, 2.3 cm distance between two plates) conformed into a hexagonal coaxial cavity (Figs. 1 and 2). We created a hexagonal coil former by cutting seven hexagonal pieces from a 6.57-mM delrin sheet and stacking them together. A 100-W computer-guided laser (Universal Laser System, Scottsdale, AZ, USA) was used to cut the delrin former. Copper foil (0.04 mM thick) was cut and attached to the delrin former. The inner conductor is made of a continuous copper sheet, while the outer conductor is made of separate plates connected with wires at each end, forming a complete end ring. Each inner plate is

¹Center for NMR Research, Department of Radiology, Pennsylvania State University College of Medicine, Hershey, Pennsylvania, USA.

²Department of Physics, Pennsylvania State University, University Park, Pennsylvania, USA.

³Center for MR Research, Department of Radiology, School of Medicine, University of Minnesota, Minneapolis, Minnesota, USA.

The review of this article was handled by an Associate Editor.

*Correspondence to: Michael B. Smith, Ph.D., Center for Nuclear Magnetic Resonance Research, Pennsylvania State University College of Medicine, 500 University Drive, Hershey, PA 17033. E-mail: mbsmith@psu.edu

Received 20 July 2004; revised 8 December 2004; accepted 14 December 2004.

DOI 10.1002/mrm.20459

Published online in Wiley InterScience (www.interscience.wiley.com).

© 2005 Wiley-Liss, Inc.

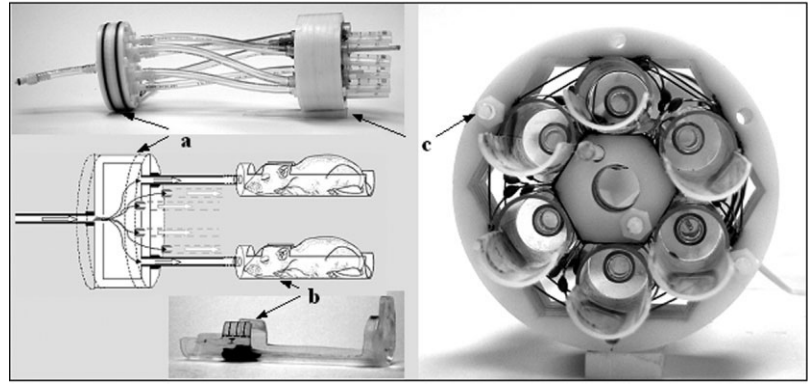


FIG. 1. Anesthesia manifold (a) and rat pup holder device (b) developed for easier positioning of 7-day-old rats. The lines represent the tubing between the anesthesia vaporizer and the manifold, and between the manifold and the rat holder. The arrows represent the gas anesthesia flow. c: Enlarged end-on view of the hexagonal coil.

connected to the corresponding outer plate with four capacitors at the four corners, making the total number of capacitors 24 for the six pairs of copper plates. Capacitor values (~24 pF) were chosen so that the coil could be tuned to resonate at 125 MHz. The tuning and matching network (52H02 Johanson capacitors, 1.5–10 pF) can be placed across any of the 24 capacitors. The space between each pair of the parallel plates is then an imaging cell with a high filling factor. All six coils are inductively coupled, and in the cyclotron mode of resonance ($m = 0$) the B_1 field is mutually shared among them. The hexagonal coil can be viewed as a coaxial cavity coil, but with a hexagonal cross-section and with the outer conductor replaced by six plates in parallel to strategically concentrate magnetic flux and reduce inhomogeneity in the radial direction.

The current distribution in the conductor plates is determined by the resonance mode of the coaxial cavity with the current flowing longitudinally in opposite directions in the inner and outer plates. Although the cylindrical coaxial cavity has inherently high sensitivity, it is accompanied by a strong B_1 field gradient along the radial direction between the inner and outer conductors (6). The hexagonal coil is designed to overcome this limitation.

Analytical Solution for the Magnetic Field

The magnetic field $\mathbf{B}(\mathbf{r})$ between the plates of the hexagonal coil can be predicted from the Biot-Savart law for the static case (8). At an arbitrary location determined by radius vector \mathbf{r} ($\mathbf{r} \neq \mathbf{r}'$), the magnetic field is given by:

$$\mathbf{B}(\mathbf{r}) = \frac{\mu_0}{4\pi} \int_{V_{hexagon}} \mathbf{j}(\mathbf{r}') \times \frac{\mathbf{r} - \mathbf{r}'}{|\mathbf{r} - \mathbf{r}'|^3} d^3r', \quad [1]$$

where $\mathbf{j}(\mathbf{r}')$ is the current density estimated as

$$\mathbf{j}(\mathbf{r}') = \left\{ \begin{array}{ll} 0, & \mathbf{r}' \notin \partial V_{hexagon} \\ \pm \frac{I}{2b} \hat{z}, & \mathbf{r}' \in \partial V_{hexagon} \end{array} \right\}, \quad [2]$$

where $\partial V_{hexagon}$ represents the surface of hexagonal coil, $V_{hexagon}$ is the volume of the hexagonal coil, I is the current through the hexagon (positive for outer plates, and negative for inner plates), $2b$ is the width of the plate, and \hat{z} is the unity vector oriented along the z -axis. Here we assume uniform current density in each plate, which is not expected to be exactly accurate at 125 MHz (9) but should still give a reasonably accurate result. The magnetic field $\mathbf{B}(\mathbf{r})$ at the arbitrary location (\mathbf{r}) is the sum of magnetic fields created by current flow in each of six outer and six inner plates:

$$\mathbf{B}(\mathbf{r}) = \sum_{j=1}^6 \mathbf{B}_{j,in}(\mathbf{r}) + \mathbf{B}_{j,out}(\mathbf{r}), \quad [3]$$

For example, current flowing through outer plate no. 1 (Fig. 2) will contribute to the magnetic field at the arbitrary point (\mathbf{r}), with the assumption that one side of the hexagon has a width of 2 cm:

$$\mathbf{B}_{1,out}(\mathbf{r}) = \frac{\mu_0}{4\pi} \int_{-b}^b dx \int_{-L}^L dz \frac{I}{2b} \hat{z} \times \frac{\mathbf{r} - \mathbf{r}'(x,z)}{|\mathbf{r} - \mathbf{r}'(x,z)|^3},$$

$$\mathbf{r}'(x,z) = \begin{pmatrix} x \\ 2.3 + \sqrt{3} \\ z \end{pmatrix} [\text{cm}], \quad [4]$$

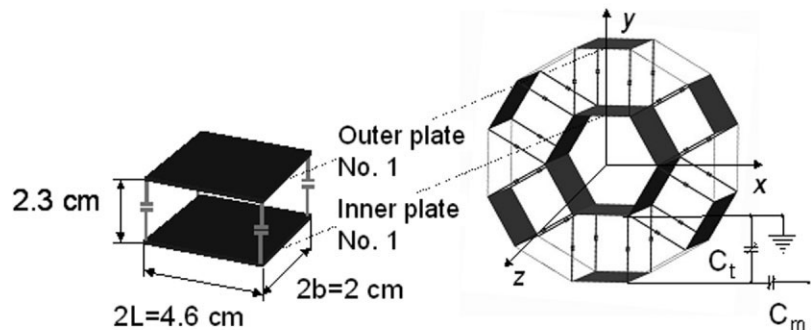


FIG. 2. Schematic drawing of the hexagonal coil discussed in the text. The tuning and matching circuit can be placed across any capacitor. One imaging cell and its dimensions are shown on the left.

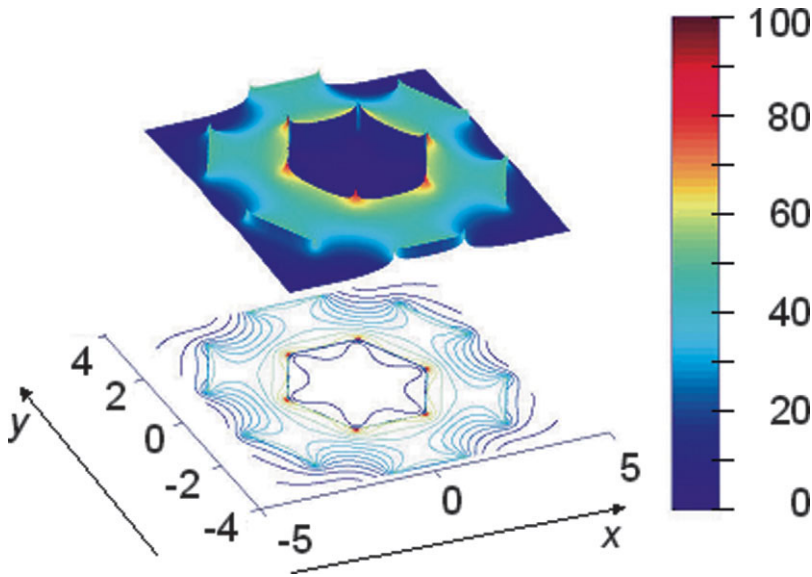


FIG. 3. The magnetic field $\mathbf{B}(\mathbf{r})$ between two plates of the hexagonal coil numerically calculated from the Biot-Savart law. The directions of the x - and y -axes are labeled on the image. Top: 3D view of the normalized magnetic field magnitude across the center of the hexagonal coil. Bottom: 2D projection of the magnetic field magnitude. Scale is given in the percentage of magnetic field magnitude (0–100%).

while current flow through inner plate no. 1 of the same imaging cell will create a magnetic field

$$B_{1,in}(\mathbf{r}) = \frac{\mu_0}{4\pi} \int_{-b}^b dx \int_{-L}^L dz \frac{-I}{2b} \hat{z} \times \frac{\mathbf{r} - \mathbf{r}'(x,z)}{|\mathbf{r} - \mathbf{r}'(x,z)|^3},$$

$$\mathbf{r}'(x,z) = \begin{pmatrix} x \\ \sqrt{3} \\ z \end{pmatrix} [\text{cm}] \quad [5]$$

at the arbitrary location (\mathbf{r}).

Integrals in the Eqs. [3]–[5] can be solved numerically for the given coil dimensions (coil length $2L = 4.6$ cm, $b = 1$ cm) with the use of MATLAB software (The Math Works, Natick, MA). The contributions to the magnetic field from the end ring wires and wires that attach capacitors to the coil are not considered by this approach. Also, the Biot-Savart law does not account for the eddy currents generated in the conductive elements of the coil. A solution for the magnetic field generated by the source currents and eddy currents, as well as the connecting wires, is discussed next using the full set of Maxwell's equations, but with some compromise in geometrical accuracy due to the method of discretization used.

Numerical Solution

We numerically calculated the magnetic field magnitude and current distribution from Maxwell's equations using the finite difference time domain method (FDTD) and commercially available software (XFDTD; REMCOM Inc., State College, PA). We modeled the coil geometry and size as closely as possible using a 160^3 mm³ 3D grid with a 2-mM cell size. A second-order Liao outer radiation boundary condition (10) was applied at the boundaries of the problem region. Capacitors were modeled as two parallel plates (2×2 mm²) with dielectric material in between. The coil was first excited with a Gaussian pulse, and from a Fourier transform of the time domain response (11) it was found to resonate at 135 MHz. We iteratively tuned the coil to

125 MHz by changing the permittivity of the dielectric material in the capacitors. Then the coil was excited with a sinusoidal 125 MHz excitation across one capacitor, as in the experiment. We performed numerical calculations for the empty coil because at 125 MHz a sample as small as a rat pup (with body dimensions of a few cm) is not expected to have a significant effect on the field distribution.

Numerical Evaluation for Factors That Contribute to B_1 Homogeneity

To determine the relative contributions of the hexagonal geometry and the discontinuity of the outer conductive element to the improved homogeneity of the hexagonal coil, we modeled coils of four different geometries: 1) two coaxial cylinders, 2) a coaxial cylinder with six arcs (30° length) in place of the outer continuous cylinder, 3) two coaxial hexagons, and 4) coaxial hexagons with six plates in place of the outer hexagon. All coils were modeled with equal length and with the same distance between the outer and inner conductors. Instead of tuning coils to 125 MHz resonant frequency, we used 12 voltage sources and a 125 MHz sinusoidal excitation in all four cases.

Coil Length Optimization

To determine the optimum length of the coil for future reference, we performed a series of numerical calculations of the B_1 field produced by hexagonal coils of different lengths, and evaluated the B_1 homogeneity of each one. We performed the calculations using the FDTD method, and the hexagonal coil was modeled such that all plates and wires were arranged as in the experimental coil, with only the model lengths being different and with 12 voltage sources (125 MHz sinusoidal excitation) instead of one. We assessed the homogeneity of each coil by analyzing the standard deviation (SD) of the B_1 field at all grid locations in a 2-cm-diameter sphere at the center of one of the compartments.

Experimental B_1 Mapping

The experimental evaluation of the coil was performed on a 3.0 T human imaging system (Medspec S300; Bruker

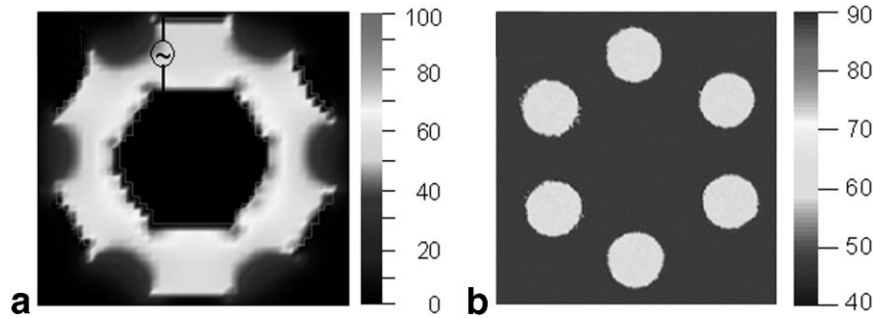


FIG. 4. **a:** Numerically calculated magnetic field between the inner and outer elements of the hexagonal coil magnitude using Maxwell's equations. The location of a single sinusoidal 125 MHz excitation is shown. The scale represents the percentage of the maximum magnetic field strength (0–100%). **b:** Experimental B_1 map. The scale represents degrees of flip angle across the imaging cell. Imaging was done using six 1.7-cm-diameter cylindrical phantoms filled with vegetable oil. The location of the voltage source is the same as in the model. From the experimental B_1 map we can conclude that flip angle distribution across the imaging cell is within 10° of the mean flip angle.

Instruments, Ettlingen, Germany) with a head gradient coil (50 mT/m gradient strength). For the experimental B_1 mapping, six 1.7-cm-diameter cylindrical vegetable oil phantoms were imaged using the gradient recalled echo (GRE) sequence with $TE = 6$ ms, $TR = 500$ ms, and a single 4-mm-thick axial slice. We calculated the flip angle (α) across the imaging cells from Eq. [6], using the SI ratio of scans with two different flip angles: α and 2α [12]

$$\alpha = \arccos\left(\frac{SI(2\alpha)}{2 SI(\alpha)}\right) \quad [6]$$

Animal Procedure

All procedures were approved by the Institutional Animal Care and Use Committee of the Pennsylvania State University College of Medicine. We developed an anesthesia manifold to evenly distribute the gas anesthesia to six animals, and a neonatal rat holder to allow easy positioning and restrict free movement of the animals (Fig. 1). An additional piece of tape (not shown) can be used to tape the animal's head to the holder. The animals were first placed in the holder and then subjected to 4% isoflurane for 2 min. After 2 min and during the imaging, anesthesia was kept at 2%.

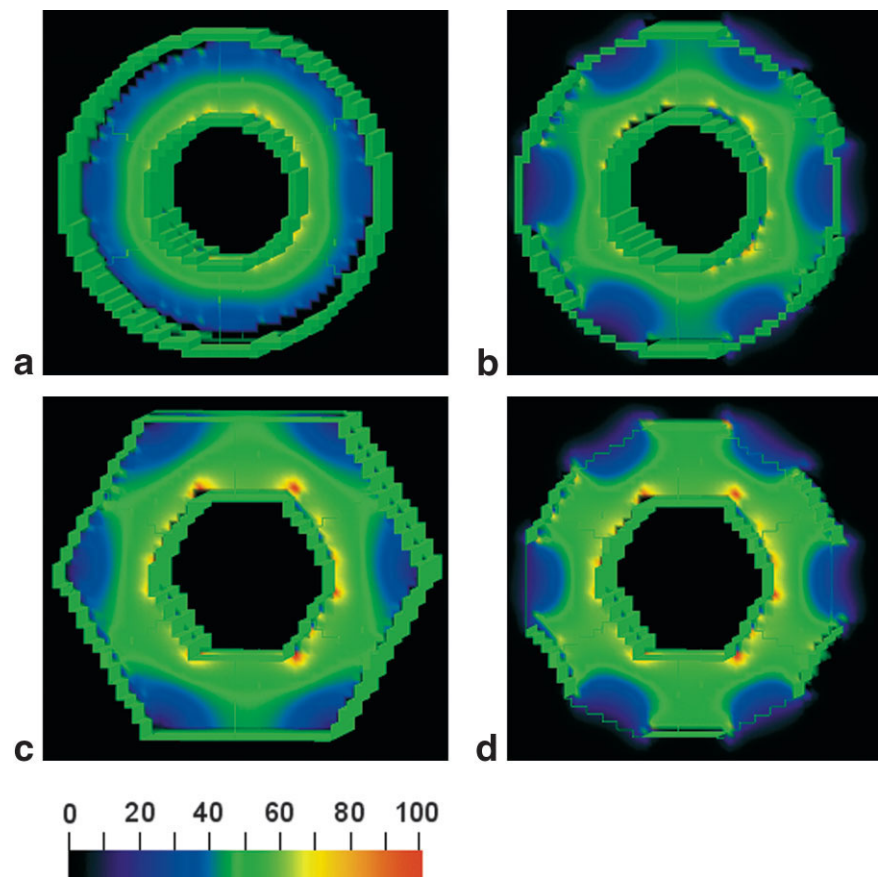


FIG. 5. The magnetic field magnitude distribution across the coaxial cylindrical coil (**a**), coaxial cylinder with six 30° long arcs instead of an outer cylinder (**b**), coaxial solid hexagonal coil (**c**), and hexagonal coil (**d**) (the outer solid hexagon is replaced with six plates arranged so that they resemble a hexagonal structure). All coils were excited with 12 sinusoidal voltage sources. The magnetic field magnitude scale is shown as the percentage of the maximum magnetic field strength (0–100%).

Imaging

A three-dimensional (3D) GRE sequence was used to acquire T_1 -weighted images of the six rat pup heads in vivo. The parameters were: TE = 10 ms, TR = 40 ms, matrix = $512 \times 512 \times 32$, FOV = $8.06 \times 8.06 \times 2$ cm³, voxel size = $157 \times 157 \times 625$ μm^3 , NEX = 1, total acquisition time = 13 min, receiver bandwidth = 57 kHz, and 2000 μs 3-lobe sinc-shaped pulses for excitation.

A multislice, multiecho spin-echo (SE) imaging sequence was used to acquire T_2 -weighted anatomical images of the six rat pup heads in vivo, with the following parameters: 11 echoes with TE = 19.4–213.51 ms, TR = 3000 ms, FOV = 8.20×8.20 cm², slice thickness = 1 mm, matrix = 512×256 , resolution = 320×160 μm^2 , NEX = 1, total acquisition time = 13 min, receiver bandwidth = 50 kHz, and 3200 μs Gaussian-shaped pulses for excitation and refocusing.

Comparison With the Single Parallel Plate Resonator

A coil made from two parallel plates (2 cm \times 4.6 cm, 2.3 cm apart), with dimensions identical to those of any single imaging cell of the hexagonal coil, was constructed for SNR comparison purposes. Six 1-mM CuSO₄-doped water phantoms (1.7 cm in diameter, 10 cm long) and six 1-mM CuSO₄-doped 50-mM saline phantoms (same dimensions as the water phantoms) were used for the SNR comparison. Imaging was done using a single-slice single-echo SE sequence (TE = 18.3 ms, TR = 3000 ms, FOV = 8.20×8.20 cm², slice thickness = 1 mm, matrix = 512×256 , NEX = 1, total acquisition time = 13 min, receiver bandwidth = 50 kHz, and 3200 μs Gaussian-shaped pulses for excitation and refocusing) that had identical parameters for imaging with both coils. To estimate sample noise and coil noise contributions to SNR, we imaged six saline phantoms with the hexagonal coil and compared the SNR of the image with SNR of the image obtained with a single saline phantom imaged with the parallel plate coil. To calculate SNR, we used the mean signal in the phantom divided by the SD of the noise in the background (13) for a region of interest (ROI) approximately the size of the phantoms. To further estimate the sample noise contribution to SNR, we compared the SNR of the image for which one saline phantom was imaged using the hexagonal coil to the SNR of the image for which six identical saline phantoms were imaged simultaneously using the same coil.

RESULTS

B_1 Field Homogeneity

The improved B_1 field homogeneity of the hexagonal coil was demonstrated by the analytical calculations, the numerical calculations, and the experimental measurements. The numerical solution predicted a 10% difference between maximal and minimal B_1 fields across the imaging cell in the hexagonal coil. The magnitude of the analytical solution found from the Biot-Savart law for $\mathbf{B}_1(\mathbf{r})$ field distribution across the center slice of the coil ($z = 0$) is given in Fig. 3. The plot presents the results of Eqs. [3]–[5] for magnetic field $\mathbf{B}(\mathbf{r})$ between two plates of the hexagonal

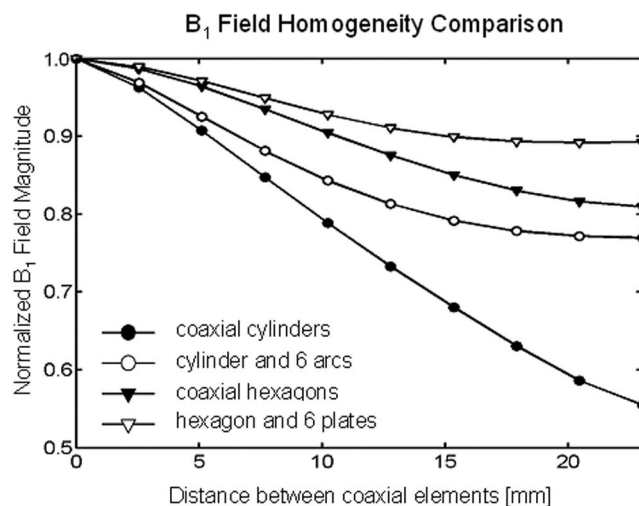


FIG. 6. B_1 field homogeneity comparison graph. The magnetic field magnitudes across the imaging cell in the case of a coaxial cylindrical coil (solid circle), a coaxial cylinder with six 30° long arcs instead of an outer cylinder (hollow circle), a coaxial solid hexagonal coil (solid triangle), and a hexagon with six plates (hollow triangle). The x-axis of the plot represents the distance orthogonal to the planes of the inner and outer elements, where zero distance is the inner wall, and 23 mm is the position of the outer wall. The y-axis is the normalized magnetic field magnitude ranging from zero to one. From the graph we can conclude that in the case of the hexagon with six plates, there is a ~10% decrease in B_1 field magnitude as we go from the inner to the outer wall. In the case of the cylindrical coil, the B_1 gradient is more prominent and there is ~45% decrease in B_1 field magnitude across the imaging cell.

coil, and displays magnetic field magnitude $|\mathbf{B}(\mathbf{r})|$. From Fig. 3 it can be concluded that the imaging space of the hexagonal coil has homogeneity within 10%. Similar results were obtained by the numerical solution of Maxwell's equation (Fig. 4a). The experimental B_1 map, acquired with six 1.7-cm oil phantoms (Fig. 4b), shows that the flip angle distribution across each imaging cell varies by less than 10°. From both numerical calculations and experimental measurements, we found that the B_1 field gradient between the inner and outer plates along a line through the center of the imaging cell is approximately 10%.

From further numerical calculations we found that four coils with different geometries have different B_1 field homogeneities. The biggest difference between maximal and minimal B_1 field magnitude was observed in the case of the coaxial cylindrical cavity coil, which was found to be 45% along a radial line through the center of an imaging cell (Figs. 5 and 6). Significant improvements in homogeneity were achieved when either the outer continuous cylinder was replaced with six arcs (each 30° long) equally spaced around the inner cylinder, or the cylindrical geometry was replaced with a hexagonal geometry (with greater homogeneity in the latter case). The continuous coaxial hexagonal coil showed a ~19% difference between the maximal and minimal B_1 field magnitudes along a radial line through the center of an imaging cell. Finally, the best homogeneity was achieved when the outer hexagon was replaced with six plates arranged so they resembled a

Table 1
Experimentally Measured Q-Values

Q-value	Empty coil	50 mM saline	100 mM saline	150 mM saline	6 rat pups
Q-value, single load	450	390	385	380	380
Q-value, six loads	450	370	315	295	310

hexagonal structure. There was a difference of only $\sim 10\%$ between the maximal and minimal B_1 field magnitudes along a radial line through the center of an imaging cell. The presence of this B_1 field gradient is due to the coaxial design.

The coil-length optimization calculation indicated that homogeneity decreased rapidly as length dropped below about 3.5 cm, and remained good at lengths greater than about 3.5 cm, with a local optimum in homogeneity (SD in a 2-cm-diameter sphere at the center of the imaging cells of only 4.30% of the mean B_1 magnitude in the sphere) at a length of 4.2 cm.

Power Requirements

When the hexagonal coil was loaded with the six cylindrical 50-mM saline phantoms, it required 0.5 dB more power than the single-cell equivalent rectangular coil loaded with one cylindrical 50-mM saline phantom to accomplish the 90° pulse during the SE experiments.

Bench Measurements

The hexagonal coil produced good B_1 field homogeneity (<1 dB difference) across the imaging cell in all six cells, as measured with the use of an HP spectrum analyzer (HP 4195A) and a small (3 mm diameter) pickup coil. The numerical values for the quality factor (Q), measured on the same spectrum analyzer (S_{11} measurement mode), for an empty coil, a coil loaded with 50–150 mM saline, and a coil loaded with six rat pups are given in Table 1.

Imaging

An axial T_1 -weighted image of six 7-day-old anesthetized rat pups is shown in Fig. 7a, and one enlarged rat pup head is shown in Fig. 7b. An SE T_2 -weighted image of six

7-day-old anesthetized rat pups is shown in Fig. 8a, and a representative enlarged image of one rat pup head is shown in Fig. 8b.

SNR

A summary of the SNR experiment is given in Table 2. As expected, the lowest SNR ratio is found in the case of the hexagonal coil loaded with six 150-mM saline phantoms. The SNR of the parallel plate coil loaded with one 50-mM saline phantom is only $\sim 5\%$ higher than the hexagonal coil loaded with six 50-mM saline phantoms.

The SNR of the hexagonal coil loaded with the single 150-mM saline phantom is only $\sim 9\%$ higher than that of the hexagonal coil loaded with six 150-mM saline phantoms. There was no difference in SNR between the single nonconductive load and six nonconductive loads when imaged with hexagonal coil.

DISCUSSION

With the proposed coil design we were able to achieve better B_1 field homogeneity than that obtained with earlier designs based on the coaxial cavity (6,7). The experimental and calculated results show good agreement. With easy tuning and matching, one can quickly examine six small animals at the same time, and good SNR can allow for a <200 μm resolution in a short period of time. The coil can fit small-aperture gradient coils, and the space in the middle can be utilized to accommodate anesthesia and temperature controls.

From the numerical calculations for B_1 magnitude across four different coil geometries, we can conclude that hexagonal geometry together with discontinuity of the outer conductor is responsible for the 35% improvement in homogeneity of the hexagonal coil compared to the cylindrical coaxial cavity coil.

To further evaluate the efficiency of increasing the imaging throughput with the hexagonal coil, we compared the SNR obtained with the hexagonal coil with that achieved by the single coil with the same dimension as one of the imaging cells of the hexagonal coil. The SNR obtained with the single parallel plate coil was only 4–5% higher than that obtained by imaging six times more samples with the hexagonal coil, in the case of a 50-mM saline load. There is little difference in SNR when the hexagonal

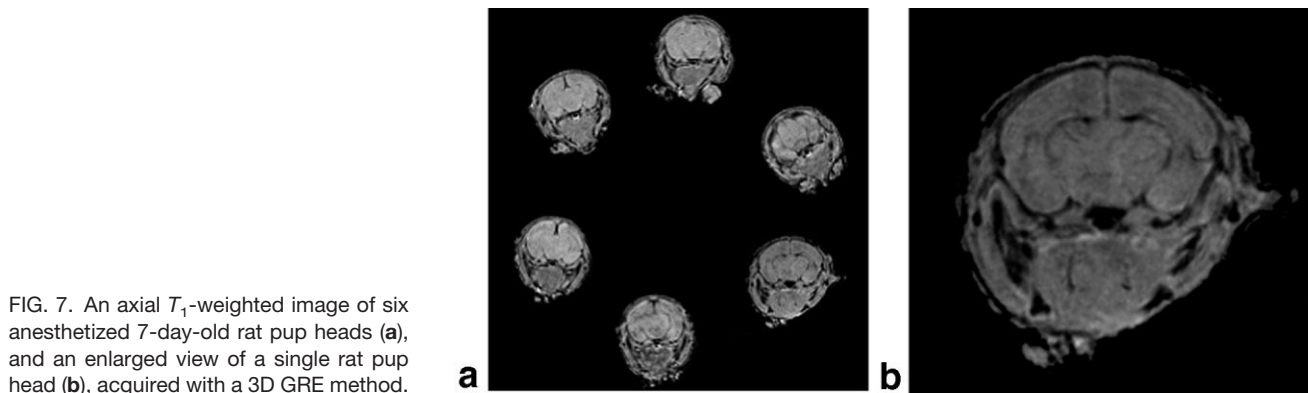


FIG. 7. An axial T_1 -weighted image of six anesthetized 7-day-old rat pup heads (a), and an enlarged view of a single rat pup head (b), acquired with a 3D GRE method.

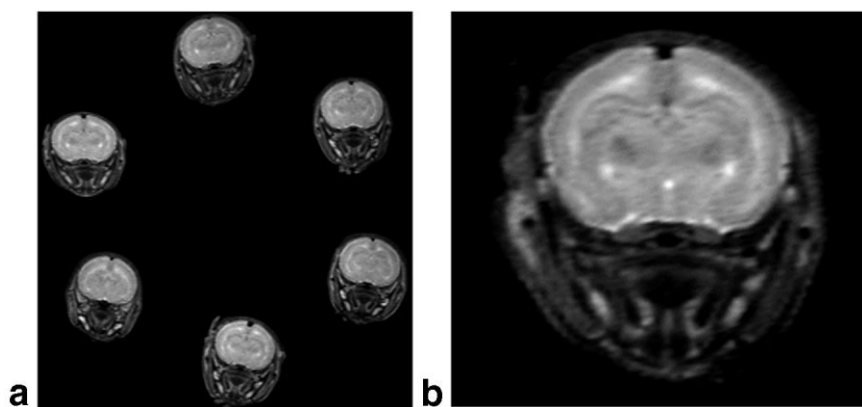


FIG. 8. An axial T_2 -weighted image of six anesthetized 7-day-old rat pup heads (a), and an enlarged view of a single rat pup head (b) acquired with a 2D SE method.

coil is loaded with one or six samples, even when the samples are conductive (Table 2). This may be because in a coil as small as this, at 125 MHz the noise is likely to be dominated by the coil rather than the sample (14). When coil noise is much larger than sample noise, SNR is proportional to the B_1 field magnitude in the sample divided by the square root of power dissipated in the coil. Because the coil noise remains constant regardless of the number of samples used, and because the same amount of signal is available from each sample, the SNR in each sample is fairly independent of the number of samples used. In addition, based on the numerical calculation, we expect SNR to improve as the coil is shortened, provided the field in the ROI remains homogeneous.

The hexagonal coil can be considered as six parallel plates connected in parallel; however, since there is non-zero current in the end rings (according to our numerical calculations, this current is 10% of the current in the wires that contain capacitors) they are connected partially in series as well. Assuming the dominance of the coil noise, the SNR measurements indicate that the coil resistance in the case of the hexagonal coil is slightly higher than that in the case of the single parallel plate coil. In the case of sample-dominated noise, SNR is proportional to the B_1 field magnitude in the sample divided by the square root of power dissipated in the sample (14). Six times more sample load in the case of hexagonal imaging would be expected to decrease SNR by $1/\sqrt{6}$ (14); however, SNR is only 4–9% lower than that obtained in the single load with the hexagonal coil using the conductive sample (Table 2), further indicating that we are in the coil-dominated noise domain. The small contributions in noise from the

samples results in a situation in which SNR is 4–9% lower for the fully loaded hexagonal coil compared to the single load situation.

With this coil in its current configuration, quadrature implementation is not available. To make additional estimates regarding SNR, we measured the induced voltage in a small pickup coil (diameter = 3 mm) for a 5-cm radius, eight-element, high-pass birdcage coil, and compared the induced voltage to the same measurement in the hexagonal coil. This is a commonly used method for estimating the sensitivity of a coil. The induced voltage in the linear 5-cm-radius birdcage coil was 1.6 mV compared to 2.7 mV in the hexagonal coil, indicating that the birdcage coil would have approximately 60% of the sensitivity of the hexagonal coil. If the birdcage coil were driven in quadrature, this would increase to 83% of the sensitivity of the hexagonal coil, but this number would decrease if the radius of the birdcage coil was increased to accommodate six small animals.

CONCLUSIONS

We have presented a novel geometry coil designed for multiple-animal imaging. The hexagonal geometry provides better homogeneity than that previously achieved with cylindrical cavity coils. The theoretical analysis was validated with experimental data and *in vivo* rat pup imaging. The discontinuity of the outer hexagonal element did not interfere with the SNR, but did improve the homogeneity of the coil. The proposed hexagonal coil design can be utilized for multiple-animal imaging with sufficient SNR, and only a single receiver is required.

ACKNOWLEDGMENTS

The authors thank Lukas Ansel for his help with the anesthesia manifold, and Justin Alder for useful suggestions. The authors would also like to thank Wanzhan Liu and Jinghua Wang for helpful discussions.

REFERENCES

- Xu S, Gade TPF, Matei C, Zakian K, Alfieri AA, Hu X, Holland EC, Soghomonian S, Tjuvajev J, Ballon D, Koutcher JA. *In vivo* multiple-mouse imaging at 1.5 T. *Magn Reson Med* 2003;49:551–557.

Table 2
Experimentally Measured SNR Values

SNR _{coil type}	1 mM CuSO ₄ water	50 mM saline +1 mM CuSO ₄	100 mM saline +1 mM CuSO ₄	150 mM saline +1 mM CuSO ₄
SNR _{rectangular coil}	263	260		
SNR _{hexagonal coil} (single phantom load)	255	253	243	237
SNR _{hexagonal coil} (six phantoms load)	255	249	230	218

2. Bock NA, Konyer NB, Henkelman RM. Multiple-mouse MRI. In: Proceedings of the 9th Annual Meeting of ISMRM, Glasgow, Scotland, 2001. p 1108.
3. Bock NA, Konyer NB, Henkelman RM. Multiple-mouse MRI. *Magn Reson Med* 2003;49:158–167.
4. Purcell EM, Torrey HC, Pound RV. Resonance absorption by nuclear magnetic moments in a solid. *Phys Rev* 1946;69:37–38.
5. Vaughan JT. RF coil for imaging system. U.S. patent 6,633,161; 2003.
6. Woelk K. Torus factor—the relationship between radiofrequency field and radial position in toroid cavity probes. *J Magn Reson* 2000;146:157–164.
7. Woelk K, Rathke JW, Klingler RJ. The toroid cavity NMR detector. *J Magn Reson A* 1994;109:137–146.
8. Jackson JD. Classical electrodynamics. 2nd ed. New York: John Wiley and Sons, Inc.; 1975. p 173.
9. Li S, Yang QX, Smith MB. RF coil optimization: evaluation of the B_1 field homogeneity using field histograms and finite element calculations. *Magn Reson Imaging* 1994;12:1079–1087.
10. Liao ZP, Wong HL, Yang BP, Yuan YF. A transmitting boundary for transient wave analyses. *Sci Sin A* 1984;27:1063–1076.
11. Kunz KS, Luebbers RJ. The finite difference time domain method for electromagnetics. Boca Raton: CRC Press; 1993.
12. Insko EK, Bolinger L. Mapping of the radiofrequency field. *J Magn Reson A* 1993;103:82–85.
13. Haacke ME, Brown RW, Thompson MR, Venkatesan R. Magnetic resonance imaging physical principles and sequence design. New York: John Wiley and Sons, Inc. 1999. p 340.
14. Edelstein WA, Glover GH, Hardy CJ, Redington RW. The intrinsic signal-to-noise ratio in NMR imaging. *Magn Reson Med* 1986;3:604–618.